Journal of Computational Physics **157,** 256–279 (2000)
doi:10.1006/jcph.1999.6374, available online at http://www.idealibrary.com on IDEAL®

Multi-Block Large-Eddy Simulations of Turbulent Boundary Layers

Andrea Pascarelli,* Ugo Piomelli,* and Graham V. Candler†

*Department of Mechanical Engineering, University of Maryland, College Park, Maryland 20742; †Department of Aerospace Engineering and Mechanics, University of Minnesota, Minneapolis, Minnesota 55455

Received December 18, 1998; revised August 30, 1999

Time-developing turbulent boundary layers over an isothermal flat plate at free-stream Mach numbers of 0.3 and 0.7 are computed using an explicit finite-difference method on structured multi-block grids. The size of each block is adjusted depending on the dimension of the largest structures present locally in the flow. This alleviates the cost of calculations in which the wall layer is resolved, and may result in substantial savings of memory and CPU time, if several layers are used. In the calculations presented the near-wall region is computed using a domain with a spanwise length $L_o^+ = 820$, which is sufficient to contain several streaks. This grid block is repeated periodically in the spanwise direction. The outer layer, which contains larger structures, is computed using a domain that is twice as wide ($L_o^+ = 1640$). Although the flow at the interface between the blocks has a periodicity length determined by the inner-layer block, within a few grid points longer wavelengths are generated. The velocity statistics and rms intensities compare well with single-block calculations that use substantially more grid points.

1. INTRODUCTION

Many technological applications involving the interaction of a fluid stream with solid boundaries result in the formation of turbulent boundary layers. For this reason, turbulent boundary layers have been considered to be one of the most important "building block" flows and have been the subject of extensive experimental, theoretical, and numerical studies.

The solid surface produces complex temporally and spatially varying flow structures, which typically have very small time and length scales in the near-wall region as compared to the overall flow scales. In incompressible flow turbulence consists of dynamically regenerating coherent structures [1]. Near the solid surface [$z^+ \leq 30$, where $z^+ = z\rho_w u_\tau/\mu_w$ is the distance from the solid surface in wall units, $u_\tau = (\tau_w/\rho_w)^{1/2}$ is the friction velocity, τ_w the shear stress, ρ_w the fluid density and μ_w the viscosity at the wall], longitudinal flow structures (streaks) are observed that have widths ranging between 20 and 80 wall units,

0021-9991/00 $35.00

and lengths that can exceed 2000 wall units. Typically, the low speed streaks are spaced about 100 wall units apart in the spanwise direction. There is substantial evidence that the streaks are generated by vortical structures, such as streamwise or quasi-streamwise vortices and "horseshoe" or "hairpin" vortices, whose dimensions scale in wall units. The turbulent motion due to these eddies is responsible for much of the Reynolds stress and turbulent kinetic energy production in boundary layers.

The region extending from the wall to $z^+ \approx 100$ encompasses the most active zone, insofar as the production of Reynolds stress is concerned. In the logarithmic layer at approximately $z^+ = 100$, there is no evidence of the streaky structures that were present at locations nearer to the wall [2, 3]. On the other hand, flow-visualization experiments and numerical simulations show that the turbulence in the outer layer, especially for $z/\delta > 0.5$ (δ being the boundary layer thickness) is intermittent, with large-scale structures interspersed between regions of irrotational flows. The scale of these structures is larger than that of the turbulence in the inner layer, although these eddies are often composed of fluid that was ejected from the near-wall region [2]. The highly irregular interface between the turbulent and non-turbulent flow exhibits three-dimensional bulges on the scale of δ both in the streamwise and spanwise directions, and narrow entrainment eddies, as observed by Robinson [1].

The different length scales of the turbulent eddies in the inner and outer layers can pose a significant challenge for numerical simulations that resolve the energy-carrying structures, such as direct and large-eddy simulations of turbulence. Chapman [4] and Reynolds [5] studied the grid requirements necessary to resolve the turbulent boundary layer. In the outer layer, the turbulent eddies scale with δ. To resolve such structures it is necessary to use a grid-spacing scaled in outer units, $\Delta x_i/\delta$. The number of grid points required to resolve the outer layer in each direction is $N_i = L_i/\Delta x_i \sim L_i/\delta$ (where L_i is the length of the computational domain). Assuming that the outer region begins at some fixed fraction of δ, and that the boundary-layer thickness scales like $Re^{-0.2}$ (where $Re = U_\infty l/\nu$ is the Reynolds number based on the free-stream velocity, U_∞, and a reference length, l, of the same order as the computational domain size, L_i), it is easy to verify that the total number of grid points required to resolve the outer layer of an attached turbulent boundary layer is proportional to $Re^{0.4}$, since $N_1 \sim Re^{0.2}$, $N_2 \sim Re^{0.2}$, and $N_3 \sim Re^0$ [4].

Since the inner-layer structures scale in wall units, the grid spacing in wall units, $\Delta x_i^+ = \Delta x_i u_\tau/\nu$, must be kept constant. This results in a number of points in each direction given by

$$N_i = \frac{L_i}{\Delta x_i} = \frac{\nu}{\Delta x_i u_\tau}\frac{L_i}{l}\frac{lU_\infty}{\nu}\frac{u_\tau}{U_\infty} = \frac{1}{\Delta x_i^+}\frac{L_i}{l}\,Re\sqrt{\frac{C_f}{2}} \sim Re^{1-\alpha}, \tag{1}$$

where it is assumed that $C_f \sim Re^{-2\alpha}$. Typical values of α are in the range $\alpha \simeq 0.1 - 0.125$, giving a total number of grid points that scales like $N = N_1 N_2 N_3 \sim Re^{2.6}$.

These scaling arguments dictate the size of computational grids that must be used by numerical simulation methods that resolve the energy-carrying turbulent flow structures. In direct numerical simulations (DNS) all of the relevant structures are resolved, down to the smallest scales of motion, and no modeling is used. In large-eddy simulations (LES), only the energy-carrying structures are computed accurately; the small, subgrid, scales, which are more isotropic and drain energy from the large scales through the cascade process, are modeled. LES can result in significant savings over DNS, in terms of computational costs, especially when no solid boundaries are present: if the grid size corresponds to a wavenumber in the inertial region of the spectrum, the resolution required by LES becomes

independent of the Reynolds number. When the energy-carrying structures are Reynolds-number dependent, as is the case in the near-wall region of a boundary layer, the cost of the calculations is again affected by the Reynolds number, and is driven by the inner-layer resolution requirements. Although significant savings can be achieved over DNS, the application of LES to high Reynolds number external flows is still expensive.

One possible approach to bypass this limitation in LES is to model the wall layer entirely. Assuming that the near-wall layer is in equilibrium, approximate boundary conditions for the wall stress can be derived using the standard logarithmic law [6–8]. Balaras *et al.* [9] introduced an alternative approach employing boundary-layer equations in attached channel and duct flows, and Cabot [10] applied this method to the separated flow behind a step. Modeling the wall layer can allow the extension of LES to flows at very high Reynolds numbers, but only at the expense of the added empiricism introduced by the approximate boundary conditions. Thus, wherever wall models do not give sufficient accuracy, the near-wall layer must be resolved.

In computational fluid dynamics there are different ways of discretizing the physical domains. Based on the connectivity, the grids can be classified as structured, unstructured, or multi-block. The most straightforward approach is the structured grid, in which connectivity information is not needed explicitly so that each mesh point is identified by indices, and the neighbors are known. While a structured grid is simple to implement and allows easy control of the order of accuracy and conservation properties of the scheme, it can result in a large number of points in regions where they are not needed. In a boundary layer, for instance, the spanwise and stremwise spacings need to be nearly constant, to satisfy the inner-layer resolution requirements discussed above. However, in the outer layer the grid spacing specified by the inner-layer resolution requirement results in an excessively fine mesh. For example, in LES calculations of channel flow, Piomelli [11] found that the grid size that corresponds to the smallest resolved structures which was barely beyond the energy-carrying range of the spectrum in the near-wall region, fell in the decaying region in the outer flow domain. Thus, for all practical purposes, the simulation was a DNS in the core of the flow. Multiple nested grids of varying resolution, as presented in [26], can also be used to resolve the near-wall motions more efficiently. Such an approach requires an inter-grid communication algorithm to advance the solution on the different meshes.

Unstructured grids allow for a local flow-dependent grid adaptation to improve the accuracy of the computation without incurring the penalties associated with global refinement. Although unstructured grids are the most flexible tool to address resolution issues, they have not yet been applied to DNS and LES very extensively, due to their higher cost, and to the difficulty in achieving high order of accuracy.

Multi-block grids, also called “macro-element” or “composite” grids, aim at combining the advantages of structured and unstructured meshes. They are based on the partitioning of the physical domain into a number of subdomains (“blocks” or “macro-elements”). On the macro-scale, the grid is composed of unstructured blocks, while within each macro-element, either an unstructured or (more commonly) a structured mesh can be used. Although less flexible than fully unstructured grids, this approach can handle more complex geometries, more efficiently, than the structured-mesh method. Furthermore, it can be extended to parallel algorithms in a straightforward manner. One disadvantage of this method is the fact that at interfaces information needs to be exchanged between blocks. This may require iterative solution of the governing equations in each block (if the solver is implicit), interpolation (if the grid points in the two blocks do not coincide), and may affect the conservation properties of the scheme.

Despite those shortcomings, by varying the size and resolution of the subdomains, a multi-block method can efficiently resolve flow fields characterized by multiple length-scales with fewer grid points than a simply connected single-block structured grid. Only block-structured (or unstructured) methods are feasible for DNS and LES of high Reynolds-number turbulent flows, since they allow the fine-grid region to be restricted to the inner layer, and the mesh to be coarsened in all directions in the outer flow. The Reynolds-number dependence of the number of mesh points is still valid, as shown by Kravchenko *et al.* [12], who performed calculations of a turbulent channel flow using a B-spline-based block-structured algorithm, and recovered Chapman's predictions [4].

The strong Reynolds-number dependence of the number of required grid points is due to the fact that the entire computational domain is discretized with a grid spacing that scales on the very small inner variables. In principle, the inner layer does not require a computational domain as large as the outer one. Jimenez and Moin [13] investigated the "minimal channel flow unit" and concluded that a computational domain that spans approximately 250–350 wall units in the streamwise direction and 100 wall units in the spanwise direction is sufficient to sustain turbulence in plane-channel flow. Thus, a computational domain of these dimensions contains a sufficient number of turbulent structures (hairpins, quasi-streamwise vortices, etc.) to allow the dynamic cycle of generation and destruction of such eddies to take its natural course.

A possible way to decrease the cost of the calculation of the inner layer in flows that are homogeneous in one direction is to use a nearly minimal flow-unit in the near-wall region that is repeated periodically, and a larger computational domain in the outer region (Fig. 1). In the spanwise and wall-normal directions, the "inner-layer unit" (ILU) would have constant dimensions in wall units. Therefore, its size (in outer variables) would scale like Re^{-1}, and it would require a constant number of grid points in the spanwise and wall-normal directions. The number of points required to resolve an ILU would be proportional to $Re^{0.9}$, since the streamwise length of the ILU is constant and the mesh in that direction still needs to be refined as the Reynolds number is increased. As the Reynolds number increases, the physical dimensions of the inner-layer unit would decrease, and the unit would be replicated as many times as necessary to match the outer flow domain (Fig. 1b). For flows that are homogeneous in two directions (such that the ILU can be repeated in the streamwise, as well as in the spanwise, direction), the cost of the ILU computation becomes independent of Reynolds number.

If one layer of ILUs interfaces directly with the outer layer block, this technique can result only in an alleviation of the cost of the simulation. For very high Reynolds numbers, in fact, there would still be a matching region between inner scales and outer scales in which the local turbulent structures scale like the distance from the wall; in this layer, the number

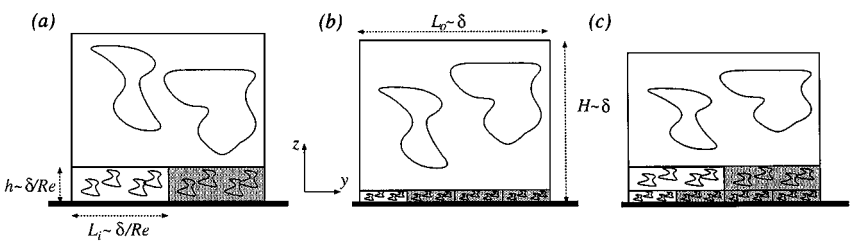

FIG. 1. Sketch of the multi-block structure in the cross-plane with "inner-layer units." The flow is out of the paper. (a) Low Reynolds number; (b) intermediate Reynolds number; (c) high Reynolds number.

of points would be proportional to

$$N \sim \int_0^{L_x} \int_0^{L_y} \int_{CRe_\tau^{-1}}^{\delta} \frac{1}{z^3}\, dz\, dy\, dx \sim Re_\tau^2. \tag{2}$$

This would still require the grid size in the outer layer to be a strong function of the Reynolds number, and the cost to be asymptotically proportional to Re_τ^2 approximately. This might still be acceptable for moderate Reynolds numbers [$Re_\tau \sim O(10^3-10^4)$], but for very high *Re* calculations, several layers would have to be employed (as sketched in Fig. 1c), with progressively increasing width and length, in order to achieve substantial savings. This could make the cost proportional to *Re* (or log *Re* for flows homogeneous in two directions) and be extremely beneficial for high *Re* calculations.

The feasibility of the proposed method hinges on the interface between the inner-layer and outer-layer domains. The largest eddy present at the interface is determined by the size of the ILU, which introduces a characteristic periodicity length into the flow. However, if some non-periodic perturbation is present in the initial conditions, lower modes (larger structures) will be generated that eventually destroy the periodicity. There will be an adjustment layer in which the flow is still characterized by the periodicity length imposed by the inner-layer unit. If the thickness of this layer is small, the proposed approach may be feasible.

In this study the feasibility of the multi-block approach proposed above will be tested, with special emphasis on the periodicity issue mentioned above, and on the continuity properties of the solution at the interface. The test-case chosen is a wall-bounded flow with two directions of homogeneity, namely a temporally developing boundary layer. This flow was chosen because it contains many of the features of importance in a spatially developing flow, which is technologically more important, but does not require special treatment of the inflow and outflow conditions. Single-block LES calculations were performed at two Mach numbers, and the results are compared with those obtained using the inner-layer unit approach. To separate the errors due to the periodicity of the inner layer from the numerical errors arising from the use of multi-block grids (interpolation, interface between subdomains) the calculations were carried out using an explicit code, with one-to-one correspondence between the domains. Studies of real flows would probably require non-conforming meshes, as well as several layers of progressively larger ILUs. With the same aim, a well-established subgrid-scale model is used, and no attempt is made to employ more advanced, and perhaps more accurate, models.

In the next section, the problem formulation, numerical method, and subgrid-scale model used are described. Then, computational results are presented and discussed. Finally, some conclusions are drawn in the last section.

2. PROBLEM FORMULATION

2.1. *Governing Equations*

The set of differential equations in Cartesian coordinates satisfied by a viscous flow in the absence of body forces reads

$$\frac{\partial \rho}{\partial t} + \frac{\partial}{\partial x_j}(\rho u_j) = 0, \tag{3}$$

$$\frac{\partial \rho u_i}{\partial t} + \frac{\partial}{\partial x_j}(\rho u_j u_i + p\delta_{ji} - \sigma_{ji}) = 0, \tag{4}$$

$$\frac{\partial \rho E}{\partial t} + \frac{\partial}{\partial x_j}[(\rho E + p)u_j - \sigma_{ji}u_i + q_j] = 0, \tag{5}$$

where the summation convention applies to repeated indices. Here, ρ is the fluid density, u_j the fluid velocity component in j direction, $E = \epsilon + u_k u_k/2$ is the total energy per unit mass (where $\epsilon = C_v T$ is the internal energy per unit mass, C_v is the specific heat at constant volume, and T the temperature), p is the thermodynamic pressure, σ_{ji} is the viscous stress tensor, and q_j is the conduction heat flux. In the present work, the fluid is assumed to be an ideal gas with constant specific heats (whose ratio is $\gamma = 1.4$). Thus, the pressure is related to ϵ by the equation of state $p = (\gamma - 1)\rho\epsilon$. The viscous stress tensor and the conduction heat flux vector are expressed as functions of the strain-rate tensor $S_{ij} = (\partial u_i/\partial x_j + \partial u_j/\partial x_i)/2$ and the temperature gradient, according to

$$\sigma_{ij} = 2\left(1 - \frac{\delta_{ij}}{3}\right)\mu S_{ij}; \qquad q_j = -k\frac{\partial T}{\partial x_j}, \tag{6}$$

where μ is the molecular viscosity, and k the thermal conductivity. The viscosity μ is assumed to depend only on temperature and is calculated using the Sutherland law

$$\mu = \mu_r \frac{T_r + T_S}{T + T_S}\left(\frac{T}{T_r}\right)^{3/2}, \tag{7}$$

where μ_r is the reference viscosity at a reference absolute temperature T_r. The thermal conductivity k is computed assuming a constant molecular Prandtl number, $Pr \equiv C_p\mu/k = 0.72$ and the constant T_S is assumed to be equal to 110.4 K [14].

2.2. *SGS Modeling*

The governing equations for LES are obtained through the application of a spatial filter to the Navier–Stokes equations to separate the effects of the (large) resolved scales from the (small) subgrid-scale motions. The filtering operation is written in terms of a convolution integral as

$$\bar{f}(\mathbf{x}, t) = \int_D G(\mathbf{x} - \boldsymbol{\xi}; \bar{\Delta})\, f(\boldsymbol{\xi}, t)\, d\boldsymbol{\xi}, \tag{8}$$

where D is the flow domain and G is some spatial filter for which

$$\int_D G(\mathbf{x} - \boldsymbol{\xi}; \bar{\Delta})\, d\boldsymbol{\xi} = 1. \tag{9}$$

The filter introduces a scale $\bar{\Delta}$, the filter width, that represents the smallest turbulence scale allowed by the filter itself. In the present calculations, the tophat filter is used in all three directions. For compressible flows, it is advantageous to use Favre-filtering [15, 16] to avoid the introduction of subgrid-scale terms in the equation of conservation of mass. A Favre-filtered variable is defined as $\tilde{f} = \overline{\rho f}/\bar{\rho}$. The resulting Favre-filtered compressible

Navier–Stokes equations of motion are given by

$$\frac{\partial \bar{\rho}}{\partial t} + \frac{\partial}{\partial x_j}(\bar{\rho}\tilde{u}_j) = 0, \tag{10}$$

$$\frac{\partial}{\partial t}(\bar{\rho}\tilde{u}_i) + \frac{\partial}{\partial x_j}(\bar{\rho}\tilde{u}_j\tilde{u}_i + \bar{p}\delta_{ij} - \tilde{\sigma}_{ji}) = -\frac{\partial \tau_{ji}}{\partial x_j} \tag{11}$$

$$\frac{\partial}{\partial t}(\bar{\rho}\tilde{E}) + \frac{\partial}{\partial x_j}[(\bar{\rho}\tilde{E} + \bar{p})\tilde{u}_j - \tilde{\sigma}_{ji}\tilde{u}_i + \tilde{q}_j] = -\frac{\partial}{\partial x_j}\left(\frac{1}{2}\mathcal{J}_j - \mathcal{D}_j + \gamma C_v Q_j\right). \tag{12}$$

Here,

$$\tilde{\sigma}_{ij} = 2\tilde{\mu}\tilde{S}_{ij} - \frac{2}{3}\tilde{\mu}\delta_{ij}\tilde{S}_{kk}, \qquad \tilde{q}_j = -\tilde{k}\frac{\partial \tilde{T}}{\partial x_j}, \tag{13}$$

where $\tilde{\mu}$ is the molecular viscosity, and $\tilde{k}$ is the thermal conductivity corresponding to the filtered temperature $\tilde{T}$. The effect of the subgrid scales appears through the SGS stresses τ_{ij}, the SGS heat flux Q_j, the SGS turbulent diffusion $\partial\mathcal{J}_j/\partial x_j$, and the SGS contribution to viscous diffusion, $\partial\mathcal{D}_j/\partial x_j$; these quantities are defined as

$$\tau_{ij} = \bar{\rho}(\widetilde{u_i u_j} - \tilde{u}_i\tilde{u}_j) \tag{14}$$

$$Q_j = \bar{\rho}(\widetilde{u_j T} - \tilde{u}_j\tilde{T}) \tag{15}$$

$$\mathcal{J}_j = \bar{\rho}(\widetilde{u_j u_k u_k} - \tilde{u}_j\widetilde{u_k u_k}) \tag{16}$$

$$\mathcal{D}_j = \overline{\sigma_{ji}u_i} - \tilde{\sigma}_{ji}\tilde{u}_j. \tag{17}$$

The equation of state has been used to express the pressure-diffusion correlation in terms of Q_j. It is also assumed here that

$$\overline{\mu(T)S_{ij}} \simeq \mu(\tilde{T})\,\tilde{S}_{ij}, \tag{18}$$

and an equivalent equality involving the thermal conductivity applies. This assumption is supported by the *a priori* study by Vreman *et al.* [17].

In the present work, the SGS stresses τ_{ij} and heat flux Q_j are modeled using the plane-averaged dynamic eddy-viscosity model [18, 19] in the form derived by Moin *et al.* [20] for compressible flows. The $\mathcal{J}_j$ and $\mathcal{D}_j$ terms are neglected. The latter assumption is supported by the *a priori* results of Martìn *et al.* [21], who examined isotropic turbulence decay at turbulent Mach number of 0.52. In their study, however, the divergence of $\mathcal{J}_j$ was found to be a significant fraction of the divergence of the SGS heat flux; thus, the first assumption may not be justified for high turbulent Mach numbers. In the present simulations, however, the turbulent Mach number is significantly smaller than that examined by Vreman *et al.* [17] and Martìn *et al.* [21] (it is of the order of 0.03–0.1), and the present assumption is acceptable, at least to test the validity of the multi-block approach.

2.3. *Numerical Scheme*

The general conservation laws can be expressed as

$$\frac{\partial U}{\partial t} = \mathcal{S}(U) \equiv -\frac{\partial F_j(U)}{\partial x_j}; \tag{19}$$

$U \in \mathbf{R}^5$ is a vector whose components are the independent variables, and $F_j = F_{cj} - F_{dj} \in \mathbf{R}^5$ is the total flux (convective and diffusive) in the x_j direction. They are defined by

$$U = \begin{Bmatrix} \bar{\rho} \\ \bar{\rho}\tilde{u}_i \\ \bar{\rho}\tilde{E} \end{Bmatrix}, \qquad F_{cj} = \begin{Bmatrix} \bar{\rho}\tilde{u}_j \\ \bar{\rho}\tilde{u}_j\tilde{u}_i + \bar{p}\delta_{ji} \\ (\bar{\rho}\tilde{E} + \bar{p})\,\tilde{u}_j \end{Bmatrix}, \qquad F_{dj} = \begin{Bmatrix} 0 \\ \tilde{\sigma}_{ji} - \tau_{ji} \\ \tilde{\sigma}_{ji}u_i - \tilde{q}_j - \gamma C_v Q_j \end{Bmatrix}; \quad (20)$$

$\mathcal{S} = \mathcal{S}_c - \mathcal{S}_d$ is the global spatial differential operator. Equation (19) is discretized by approximating U as $U^n_{i,j,k}$ at location $(i\Delta x_1, j\Delta x_2, k\Delta x_3)$ and time $t^n = n\Delta t$, and solved numerically.

To resolve properly the details of the boundary layer, the grid points are clustered near the wall in the wall normal direction (z) while the spacing in x and y is kept uniform. The numerical solutions are computed on a uniform grid in computational space (ξ, η, ζ). The transformation relations from physical space (x, y, z) to the computational space are

$$x = \xi, \qquad y = \eta, \qquad z = z(\zeta) \quad (21)$$

and the wall-normal derivatives are computed in the regular ζ-space, e.g.,

$$\frac{\partial f}{\partial z} = \frac{\partial f}{\partial \zeta}\frac{d\zeta}{dz}, \qquad \frac{\partial^2 f}{\partial z^2} = \frac{\partial f}{\partial \zeta}\frac{d^2\zeta}{dz^2} + \frac{\partial^2 f}{\partial \zeta^2}\left(\frac{d\zeta}{dz}\right)^2, \text{ etc.}$$

The Favre-filtered Navier–Stokes equations (10)–(12) thus become

$$\frac{\partial U}{\partial t} + \frac{\partial F}{\partial \xi} + \frac{\partial G}{\partial \eta} + \frac{\partial H}{\partial \zeta}\frac{d\zeta}{dz} - \frac{\partial F_d}{\partial \xi} - \frac{\partial G_d}{\partial \eta} - \frac{\partial H_d}{\partial \zeta}\frac{\partial \zeta}{dz} = 0, \quad (22)$$

where $F = F_{c1}$, $G = F_{c2}$, $H = F_{c3}$, and a similar notation is used for the diffusive fluxes.

Let L_x, L_y, L_z be the dimensions of the computational domain Ω in the x, y, z directions, respectively. For the discretization of Ω, let

$$x_i = \xi_i \Delta x \qquad (\xi_i = i - 1),\ i = 1, \ldots, nx \quad (23)$$

$$y_i = \eta_j \Delta_y \qquad (\eta_j = j - 1),\ j = 1, \ldots, ny \quad (24)$$

$$z_1 = 0, \qquad z_k = \frac{1 - \alpha^{\zeta_k}}{1 - \alpha}\Delta z_1 \quad (\zeta_k = k - 1),\ k = 2, \ldots, nz, \quad (25)$$

where $\Delta x = L_x/(nx - 1)$, $\Delta y = L_y/(ny - 1)$, and nx, ny are the number of grid points in the x, y directions, respectively. A Cartesian non-uniform grid with nz points stretched with geometric progression in the wall-normal direction is used; $\alpha = \Delta z_{k+1}/\Delta z_k$ is the constant ratio of successive intervals, with $\Delta z_k = z_{k+1} - z_k$.

The numerical approximation to the spatial operator $\mathcal{S}_c(u)$ is

$$\mathcal{S}_c(u) = -\left[\left.\frac{\delta F}{\delta x}\right|_{i,j,k} + \left.\frac{\delta G}{\delta y}\right|_{i,j,k} + \left.\frac{\delta H}{\delta z}\right|_{i,j,k}\left(\frac{d\zeta}{dz}\right)_{z=z_k}\right], \quad (26)$$

where $\delta f/\delta x_l$ denote a finite difference operator acting on f with respect to x_l.

The approximation of the convective flux derivatives in the Navier–Stokes equations is a key element of the spatial integration. Here, the discrete operator calculations are independent in x, y, and z directions. For example, $\delta F/\delta x|_{i,j,k}$ is calculated componentwise holding indices j and k fixed, i.e., along a slice of data in the x-direction. A fourth-order accurate scheme is used, in which the first derivative is constructed as the weighted sum of a central-difference method and an upwind-biased method. This approach yields a scheme with good modified wavenumber performance and a small level of dissipation at high wavenumbers. Denoting $F_{i,j,k}$ as the discrete approximation of the convection flux F at $(i\Delta x_1, j\Delta x_2, k\Delta x_3)$, the x-direction derivative is given by

$$\left.\frac{\delta F}{\delta x}\right|_{i,j,k} = \frac{1}{\Delta x}\left[\frac{1}{180}(F_{i+2,j,k} - F_{i-2,j,k}) - \frac{2}{9}(f_{i+1,j,k} - F_{i-1,j,k}) + \frac{64}{45}\left(F_{i+\frac{1}{2},j,k} - F_{i-\frac{1}{2},j,k}\right)\right], \tag{27}$$

where, in order to find a 4th-order solution, it is required that

$$F_{i+\frac{1}{2},j,k} = F\left(U_{i+\frac{1}{2},j,k}\right) + O(\Delta x^5). \tag{28}$$

The $F_{i\pm 1/2,j,k}$ are calculated by an upwind-biased method; the flux F is decomposed as

$$F(U) = F^+(U) + F^-(U), \tag{29}$$

where $F^{\pm}(U) = A^{\pm}(U)U$ and $A^{\pm}(U)$ are such that $A = A^+ + A^-$ and $\pm A^{\pm}(U)$ have real and non-negative eigenvalues. The flux-vector-splitting method of Steger and Warming [22] is employed. The high-order accuracy of the scheme is achieved by evaluating each component of the conserved variables at cell interfaces $U_{i+1/2,j,k}$ with a 5th-order accurate spatial interpolation of the node values. The resulting numerical flux function is

$$F_{i+\frac{1}{2},j,k} = F^+_{i+\frac{1}{2},j,k} + F^-_{i+\frac{1}{2},j,k}, \tag{30}$$

where

$$F^+_{i+\frac{1}{2},j,k} = \frac{A^+_{i+\frac{1}{2},j,k}}{128}(3U_{i-2,j,k} - 20U_{i-1,j,k} + 90U_{i,j,k} + 60U_{i+1,j,k} - 5U_{i+2,j,k}) \tag{31}$$

$$F^-_{i+\frac{1}{2},j,k} = \frac{A^-_{i+\frac{1}{2},j,k}}{128}(-5U_{i-1,j,k} + 60U_{i,j,k} + 90U_{i+1,j,k} - 20U_{i+2,j,k} + 3U_{i+3,j,k}). \tag{32}$$

All the values required for the evaluation of the Jacobian matrices $A^{\pm}_{i+1/2,j,k}$ are interpolated across six grid points. For example, the speed of sound, a, is calculated as

$$a_{i+\frac{1}{2},j,k} = (3a_{i-2,j,k} - 25a_{i-1,j,k} + 150a_{i,j,k} + 150a_{i+1,j,k} - 25a_{i+2,j,k} + 3a_{i+3,j,k}). \tag{33}$$

The terms $\delta G/\delta y|_{i,j,k}$ and $\delta H/\delta z|_{i,j,k}$ in (26) are treated similarly. The modified wavenumber properties of this conservative scheme are comparable to those of the nonconservative method of Rai, Gatski, and Erlebacher [27] that was used for the simulation of a spatially evolving compressible boundary layer.

For the compressible Navier–Stokes equations (19) in a conservation-law form, the second-order derivatives appear as first-order derivatives of the transport flux vectors F_{dj}. These terms can be discretized in many ways, independently of $\partial F_{cj}/\partial x_j$. Here, the discretization of the diffusive terms is carried out using a fourth-order-accurate centered difference method. For example, the first and second derivatives of f with respect to x are given by

$$\left(\frac{\partial f}{\partial x}\right)_{i,j,k} = \frac{-f_{i+2,j,k} + 8f_{i+1,j,k} - 8f_{i-1,j,k} + f_{i-2,j,k}}{12\Delta x} + O(\Delta x^4) \tag{34}$$

$$\left(\frac{\partial^2 f}{\partial x^2}\right)_{i,j,k} = \frac{-f_{i+2,j,k} + 16f_{i+1,j,k} - 30f_{i,j,k} + 16f_{i-1,j,k} - f_{i-2,j,k}}{12\Delta x^2} + O(\Delta x^4). \tag{35}$$

The y-derivatives are obtained in the same manner. Owing to the treatment of the viscous terms, the formal spatial accuracy of the global scheme is fourth order.

Replacing the spatial derivatives with the above approximations yields a set of the equations of the form

$$\frac{dU_{i,j,k}}{dt} = \{\tilde{\mathcal{S}}[U(t)]\}_{i,j,k}, \tag{36}$$

where $\tilde{\mathcal{S}}$ is a 4th-order discrete approximate to the spatial operator in (19). Equation (36) is a set of time-continuous coupled ordinary differential equations and any integration scheme applicable to ODEs may be used. In general, explicit schemes are limited to a short time-step owing to stability limitation; however, the implementation of the discretized equations in a multi-block format (see below) is simplified when an explicit time advancement is adopted. For this reason, an explicit third-order low-storage Runge–Kutta method [23] was used for these calculations.

The fourth-order finite-difference scheme described above requires modifications for the treatment of the non-periodic boundaries. The code adopts a fourth-order central differencing at points $k = 3$ and $k = nz - 2$ and reduces to second-order central scheme at points $k = 2$ and $k = nz - 1$ for the convective and diffusive terms. Care was taken to maximize the accuracy of the method at the near-wall points, while maintaining the stability of the scheme; higher-order extrapolations make the scheme unstable [28].

2.4. *Initial and Boundary Conditions*

The initial condition was obtained from a single-block large-eddy simulation of the incompressible turbulent flat-plate boundary layer. Uniform density and temperature fields were specified. The Reynolds number was $Re_{\delta_o^*} = \delta_o^* U_\infty/\nu \approx 1110$, where δ_o^* is the initial displacement thickness. The size of the computational domain was $120\delta_o^* \times 30\delta_o^* \times 22\delta_o^*$ in the streamwise, spanwise, and wall-normal directions, respectively; these dimensions corresponded to $6570 \times 1640 \times 1230$ wall units.

Periodic boundary conditions were used in the streamwise and spanwise directions, and isothermal no-slip conditions were specified at solid surface, $z = 0$. The plate temperature T_w was set equal to the free-stream temperature T_∞. The wall density was computed from conservation of mass at the wall,

$$\frac{\partial \rho}{\partial t} = -\left[\frac{\partial(\rho w)}{\partial z}\right]_w, \tag{37}$$

and, along with the specified wall temperature T_w, was used to calculate the wall pressure using the equation of state. The wall-normal derivative in (37) was approximated by a second-order-accurate formula. At the top of the domain, the normal gradients of the conserved variables were set to zero.

The use of periodic boundary conditions implies that the boundary layer develops in time, rather than in the streamwise direction. To simulate properly a spatially developing boundary layer, either inflow–outflow conditions must be used, or some other approximate technique, such as the "fringe method" [24] must be adopted. Since the purpose of the present calculation is to test the ILU concept, it was preferred not to introduce additional uncertainties. Although this configuration is not the exact equivalent of a flat-plate boundary layer, it contains many of the important physical features of that flow (inner- and outer-layer scalings, for instance). Thus, it constitutes a consistent test case for the comparison of single- and multi-block calculations.

2.5. *Block Partitioning and Grid Distribution*

Two types of calculations were performed; first, single-block computations were carried out as baseline cases; then, multi-block computations were performed to validate the proposed approach. In the single-block cases, $64 \times 48 \times 48$ grid points were used in the streamwise, spanwise, and wall-normal directions, respectively, to discretize a domain whose size was equal to that of the initial field ($120\delta_o^* \times 30\delta_o^* \times 22\delta_o^*$); this resulted in an initial grid resolution $\Delta x_o^+ \approx 103$, $\Delta y_o^+ \approx 34$, and $\Delta z_{min,o}^+ = 0.15$ (a subscript o indicates that the initial friction velocity, $u_{\tau,o}$, and displacement thickness, δ_o^*, were used for the normalizations).

The multi-block calculations were carried out using the arrangement shown in Fig. 2. Three rectangular subdomains were used, with conforming grids (the grid lines were continuous across the interfaces). Interface and boundary conditions were specified by using four "ghost points" to ensure that fourth-order accuracy was achieved even at the sub-domain interfaces. These additional cells are filled at the start of each time step level

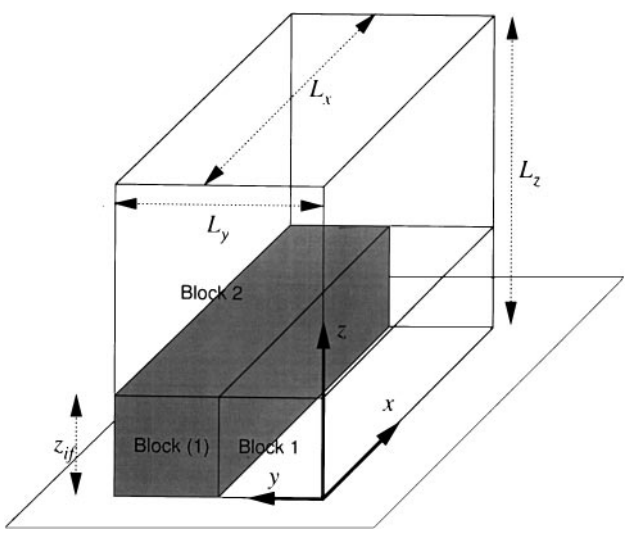

FIG. 2. Multi-block arrangement for 3D turbulent boundary layer.

TABLE I
Grid Resolutions

	$z_o^+ = 30$	$z_o^+ = 104$
Inner layer	$64 \times 24 \times 24$	$64 \times 24 \times 32$
Outer layer	$64 \times 48 \times 24$	$64 \times 48 \times 16$

in a manner that depends on the geometrical (internal or external interface) and physical (wall, freestream, periodicity) nature of the boundary condition.

The inner layer was discretized using two subdomains, Blocks 1 and (1) in Fig. 2; the latter is purely virtual and is a periodic copy of Block 1. The inner-layer unit had the same dimension in the streamwise direction as the single-block calculation and extended up to a height z_{if}, which could be varied. Its spanwise size was $L_{y,o}^+ = 820$. The dimensions of the ILU were significantly larger than those of the "minimal flow unit" of Jimenez and Moin [13] and were sufficient to contain several near-wall structures. The outer layer was discretized using a single block (Block 2 in the figure), whose dimensions were $L_{x,o}^+ = 6570$, $L_{y,o}^+ = 1640$; in the wall normal direction, it extended from z_{if}^+ to $L_{z,o}^+ = 1230$. Two values of z_{if} were tested: in one case, the interface was placed in the buffer region, at $z_o^+ = 30$, in the other, in the logarithmic layer at $z_o^+ = 104$. The grids used for the two cases are summarized in Table I.

For the multi-block calculations, the initial condition had to modified to ensure regularity at the interface between the virtual inner-layer block and the outer block. This was achieved by assigning a generic variable q at point $y + L_y/2$ to be the average of the same variable in the single-block calculation, q_s, at points y and $y + L_y/2$. An exponentially decaying function of z was used to decrease the contribution of the point y as z increased,

$$q(x, y + L_y/2, z, 0) = [1 - g(z)]\, q_s(x, y, z, 0) + g(z)\, q_s\left(x, y + \frac{L_y}{2}, z, 0\right)$$
$$\forall\, 0 \le x \le L_x, 0 \le y \le L_y/2, z_{if} \le z \le L_z, \quad (38)$$

where $g(z)$ is defined as

$$g(z) = \frac{1}{\tanh(\beta)} \tanh\left[\frac{\beta(z - z_{if})}{L_z - z_{if}}\right]. \quad (39)$$

The choice of the interface location z_{if} and of the parameter β, which controls the thickness of the region over which the function transitions from 0 to 1, may affect the results significantly, as will be shown later.

3. RESULTS AND DISCUSSION

Large-eddy simulations were carried out for two values of the Mach number, $M_\infty = 0.3$ and $M_\infty = 0.7$. The mean flow temperature and density were chosen to be $T_\infty = 300$ K and $\rho_\infty = 1$ kg/m^3. In the viscosity law, $T_r = 273$ K, and the reference viscosity was $\mu_r = 1.71 \times 10^{-5}$ kg/(m · s) and $\mu_r = 3.99 \times 10^{-5}$ kg/(m · s) for the two calculations, respectively. The Reynolds numbers per unit length ($Re/l_r = 5.66 \times 10^6$ m^{-1}) was maintained constant while the Mach number was changed.

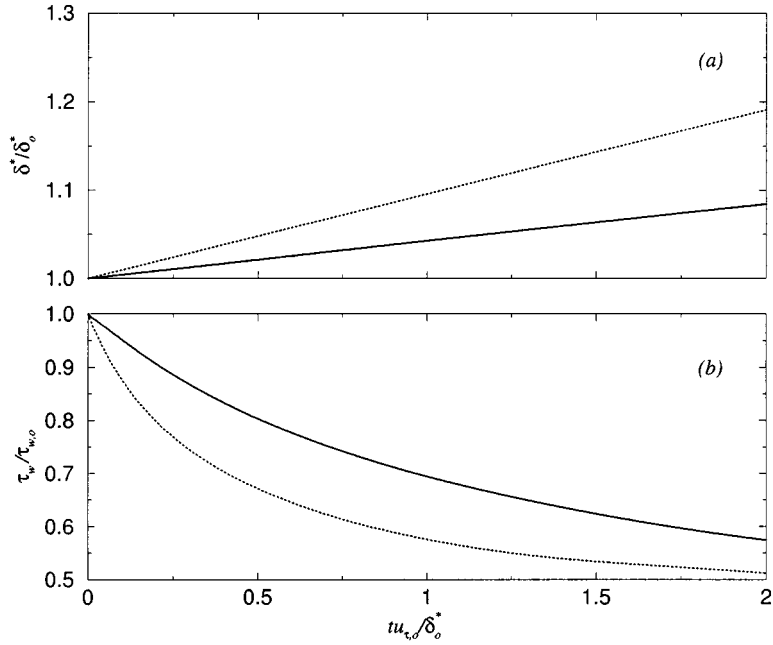

FIG. 3. Time history of non-dimensional boundary layer displacement thickness and shear stress at the wall. —, $M = 0.3$; $\cdots$, $M = 0.7$.

As mentioned in Subsection 2.4, the adoption of periodic boundary conditions implies that the boundary layer is growing in time, rather than in space. Figure 3 shows the time-evolution of the displacement thickness δ^* and wall stress τ_w for the single-block calculations. The simulation was stopped when the boundary layer thickness became comparable with the height of the computational domain, after approximately 2.5 LETOTs. Over this period, the wall stress decreased by half, and the friction velocity by 30%; thus, the Reynolds number based on δ^*, u_τ and ν ranged from 55 to 45 for the low Mach number case, and from 55 to 47 in the high Mach number calculation.

Figure 4 shows the profiles of the plane-averaged mean velocity, $u^+ = \langle u \rangle / u_\tau$ and trace of the resolved Reynolds stresses, $\langle q^2 \rangle = \langle u_i'' u_i'' \rangle$ (where $u_i'' = \overline{u}_i - \langle \overline{u}_i \rangle$ and $\langle \cdot \rangle$ indicates an average over the two homogeneous directions) obtained from the single-block calculations at the times corresponding to $Re_{\delta^*} = U_\infty \delta^* / \nu = 2230$. The instantaneous friction velocity is used to normalize both quantities. A well-defined logarithmic layer is observed in both cases, although its intercept is higher (approximately 7, instead of the standard value of 5.2) due to the low resolution used, which results in an overestimation of the thickness of the wall layer, and in a lower value of the wall stress τ_w. Correspondingly, high values of $\langle q^2 \rangle$ are observed.

Several multi-block calculations, whose parameters are summarized in Table II, were compared with the single-block calculations. The multi-block calculations differed by the height of the interface between the two layers, and by the thickness of the transition layer (i.e., by the parameter β). In addition, in two of the calculations the initial condition was modified by adding a random noise component to match the initial plane-averaged Reynolds stress distribution. The weighted-average procedure described in Subsection 2.4 results in a defect in the plane-averaged Reynolds stresses equal to

$$\Delta \langle u_i'' u_j'' \rangle = 2g(z)[1 - g(z)] \langle u_i'' u_j'' \rangle. \tag{40}$$

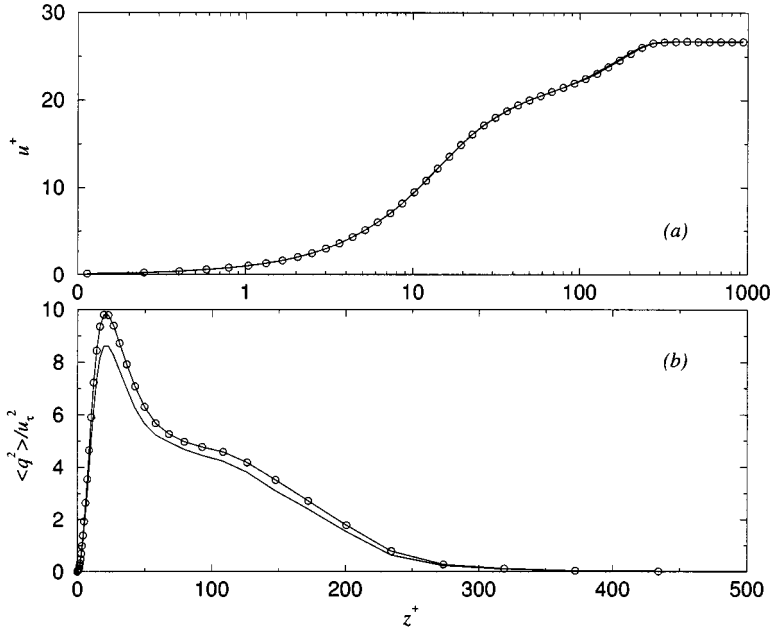

FIG. 4. Mean velocity profiles and trace of the resolved Reynolds stresses at $Re_{\delta^*} = 2230$. Lines, $M = 0.3$; lines with symbols, $M = 0.7$.

To correct this defect, a procedure similar to that used by Lund *et al.* [25] to generate inflow conditions for spatially developing simulations was followed. At each vertical location, three sequences of random numbers with zero mean, unit variance, and zero covariance with the other two distributions were generated. These uncorrelated random fluctuations were then scaled and combined to match $\Delta\langle u_i'' u_j''\rangle$. The resulting signals were added to each component of the velocity field. This procedure has two effects: first, it gives an initial condition whose second-order statistics match exactly those of the single-block calculation; second, the random fluctuation scrambles somewhat the initial periodicity of the flow at the interface; this was expected to be beneficial in decreasing the thickness of the transition layer. As will be shown later, this correction proved ineffectual because the uncorrelated random noise was rapidly dissipated.

In Fig. 5 the mean velocity profiles after 1 LETOTs are shown. Practically no difference can be observed between the various cases at this time. The same behavior is obtained at later times for this case, as well as for the higher Mach-number case.

TABLE II
Summary of Simulation Parameters

Case	M	$z^+_{if,o}$	Parameters
003	0.3	—	Single block
103	0.3	30	Thick transition ($\beta = 15$)
203	0.3	30	Thin transition ($\beta = 90$)
303	0.3	30	Thin transition ($\beta = 90$), random noise correction
403	0.3	104	Thin transition ($\beta = 90$), random noise correction
007	0.7	—	Single block
307	0.7	30	Thin transition ($\beta = 90$), random noise correction

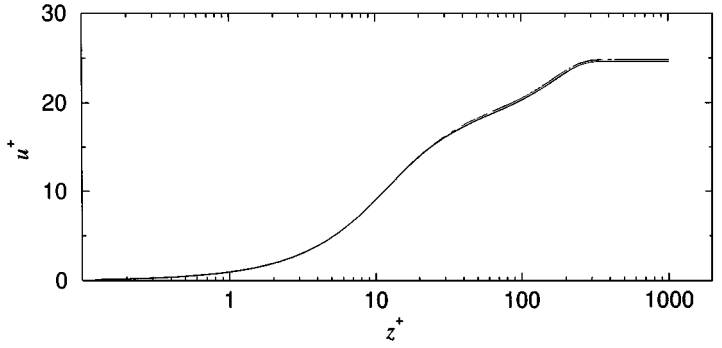

FIG. 5. Mean velocity profiles at $tu_{\tau,o}/\delta_o^* = 1$ for $M = 0.3$. —, single block; $\cdots$, $z^+_{if,o} \approx 30$ wide transition; ---, $z^+_{if,o} \approx 30$ narrow transition; – – –, $z^+_{if,o} \approx 30$ narrow transition and random noise; – - –, $z^+_{if,o} \approx 104$ narrow transition and random noise.

Figure 6 shows the rms turbulence intensities, $u_{i,rms} = \langle u_i''^2 \rangle^{1/2}$, for the low Mach-number case at $tu_{\tau,o}/\delta_o^* = 1$. The defect due to the intialization procedure is particularly evident in the spanwise fluctuations (Fig. 6b), but by $z^+ \approx 60$ the fluctuations are again fairly accurate. The effect of the initial conditions persisted for the entire period studied; even after 2.5 LETOTs a small defect was observed. Since the calculation had to be stopped at that time, it could not be verified whether (as one would expect) in a steady-state case the flow would eventually lose the memory of the initial condition. In the wide-transition calculation the defect extends to a thicker region (roughly, $30 < z^+ < 150$). Overall, the most accurate results were obtained when the interface was placed in the logarithmic region.

The addition of the random noise, as mentioned before, did not improve the results: although at $tu_{\tau,o}/\delta_o^* = 0$ the rms profiles match exactly those of the single-block calculations,

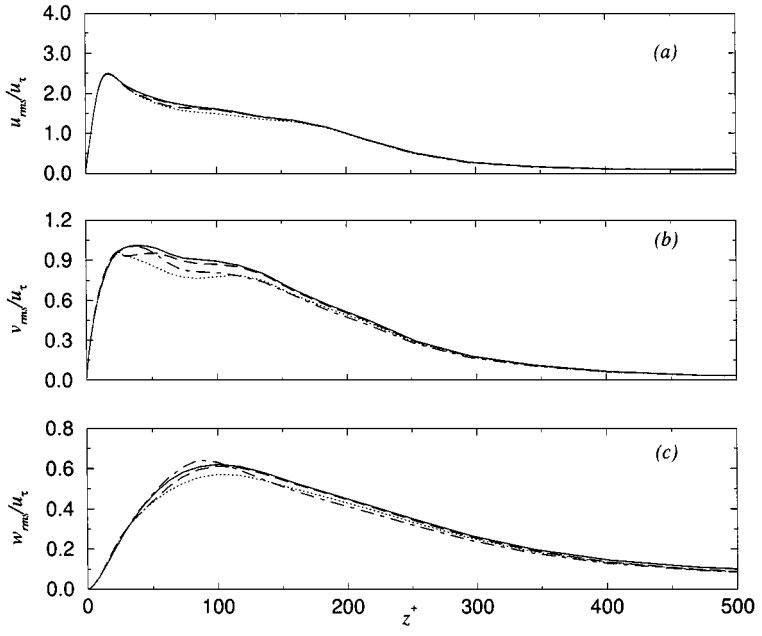

FIG. 6. Turbulence intensities at $tu_{\tau,o}/\delta_o^* = 1$ and $M = 0.3$. (a) Streamwise, (b) spanwise, (c) wall normal. —, single block; $\cdots$, $z^+_{if,o} \approx 30$, wide transition; – – –, $z^+_{if,o} \approx 30$, narrow transition; – - –, $z^+_{if,o} \approx 104$, narrow transition.

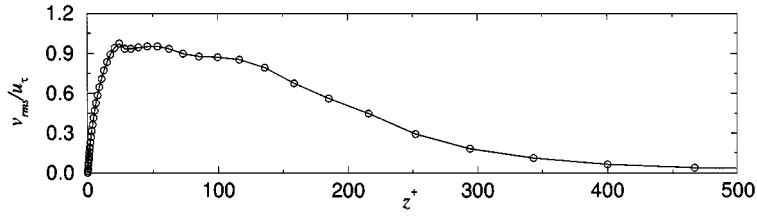

FIG. 7. Spanwise turbulence intensity at $tu_{\tau,o}/\delta_o^* = 1$ and $M = 0.3$; $z_{if,o}^+ \approx 30$. —, narrow transition; ○, narrow transition and random noise.

the random noise component is quickly dissipated. For example, at $tu_{\tau,o}/\delta_o^* = 1$ calculations with and without random noise give the same results, as shown in Fig. 7.

The resolved Reynolds shear stress, $-\langle \rho u'' w'' \rangle$ normalized by τ_w, is shown in Fig. 8 for the $M = 0.3$ calculation. The differences observed in the rms intensities are more evident here. The calculations in which the interface is in the buffer layer underpredict the stress throughout the buffer and logarithmic regions; more accurate prediction of the stresses is obtained when the interface is in the logarithmic region. The maximum contribution of subgrid-scale shear stresses on the resolved ones is about 8% of the shear stress at the wall.

At the higher Mach number (Fig. 9), similar results are obtained. However, the agreement is better, even for an interface in the buffer layer. This result may be due to the fact that at higher Mach number the convection effects are more significant, and stronger non-linear interactions scramble the initial periodicity more rapidly.

The first- and second-order statistics obtained using the multi-block approach with a periodic inner-layer unit compare well with those of single-block calculations at both Mach numbers examined. The main effect of the interface on the results is due to the initialization procedure, which results in a Reynolds-stress defect that was not recovered by the time the calculation was stopped. One could conjecture that if the flow were statistically steady, and enough time were given for the nonlinear interactions, the defect would be completely filled in; the high-Mach number results support this argument. In any case, when the interface is located in the logarithmic layer this defect is rather small, and good agreement with the single-block calculations is achieved.

The effect of the interface periodicity on the turbulence structure in the outer layer remains to be investigated. To this end, define the two-point autocorrelation of an arbitrary

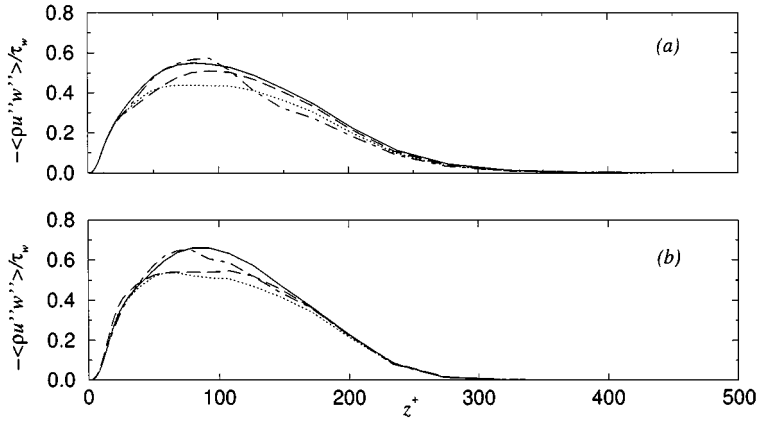

FIG. 8. Resolved Reynolds shear stress for $M = 0.3$. (a) $tu_\tau/\delta^* = 0.4$; (b) $tu_\tau/\delta^* = 2$. —, single block; · · ·, $z_{if,o}^+ \approx 30$, wide transition; ---, $z_{if,o}^+ \approx 30$, narrow transition; – - –, $z_{if,o}^+ \approx 104$ narrow transition.

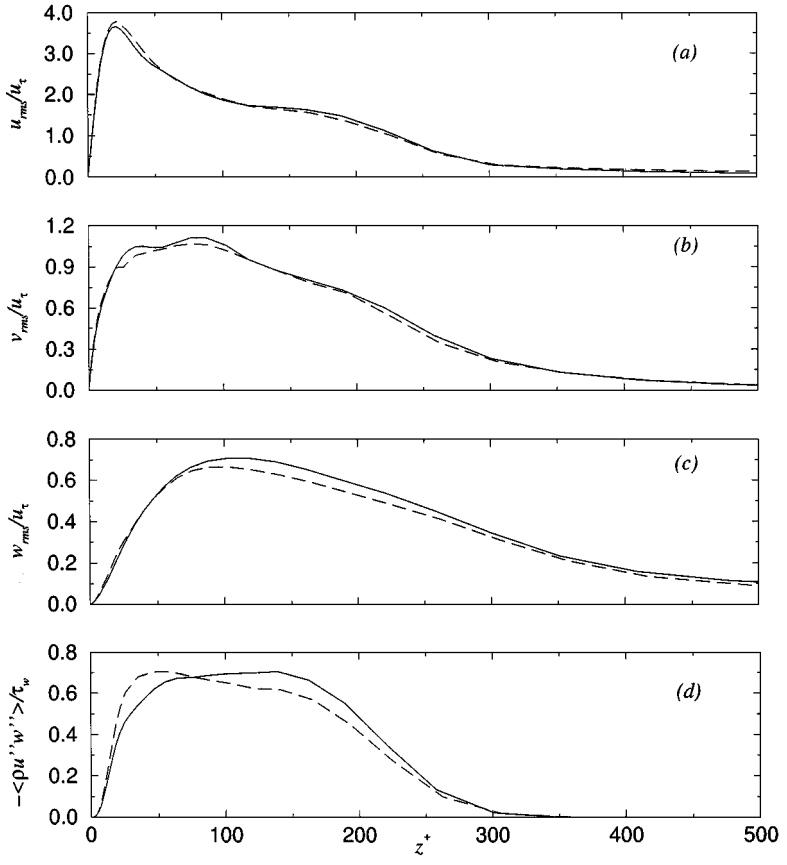

FIG. 9. Turbulence intensities and Reynolds shear stress at $tu_{\tau,o}/\delta_0^* = 2$ and $M = 0.7$. (a) Streamwise rms, (b) spanwise rms, (c) wall normal rms, (d) Reynolds shear stress. —, single block; – – –, $z_{if,o}^+ \approx 30$, narrow transition.

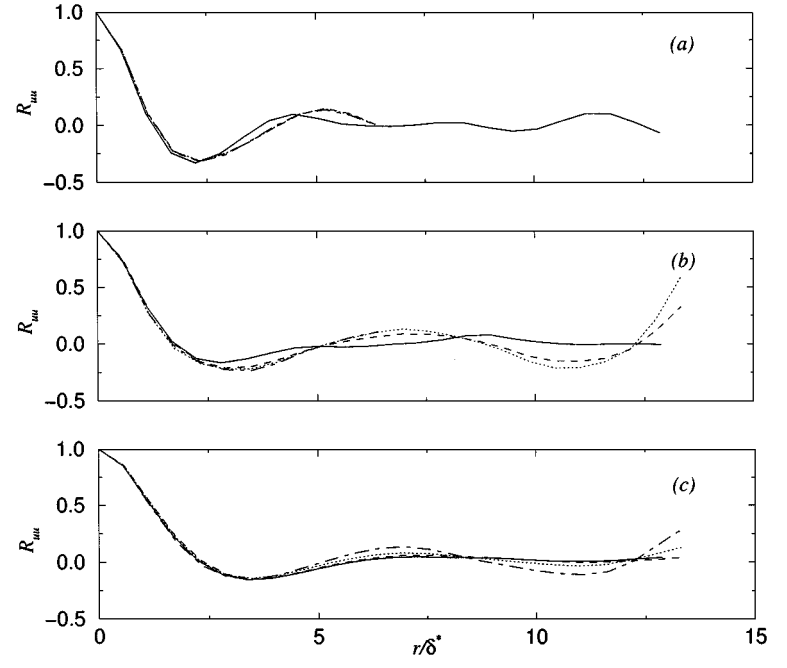

FIG. 10. Two-point spatial autocorrelation function R_{uu} at $tu_{\tau,o}/\delta_o^* = 1$ for M = 0.3. (a) $z_o^+ \approx 10$, (b) $z_o^+ \approx 35$, (c) $z_o^+ \approx 167$. —, single block; · · ·, $z_{if,o}^+ \approx 30$ wide transition; ---, $z_{if,o}^+ \approx 30$ narrow transition; – - –, $z_{if,o}^+ \approx 104$ narrow transition.

fluctuating velocity component q'',

$$R_{qq}(r, z; t) = \frac{\langle q''(x, y, z; t) q''(x, y + r, z; t)\rangle}{\langle q''(x, y, z; t)^2\rangle}. \tag{41}$$

The streamwise-velocity autocorrelation is shown in Fig. 10 at $tu_{\tau,o}/\delta_o^* = 1$, and at three distances from the wall (normalized using $u_{\tau,o}$). At $z_o^+ \approx 10$, the two-point correlation goes to zero well before half of the sub-domain width, showing that the width of the ILU is sufficient to include the widest structures present in the flow. Incidentally, the negative peak of the two-point correlation corresponds to an average streak spacing of $\lambda^+ \approx 200$, twice the experimental value; this result is consistent with the high intercept of the logarithmic layer and the thicker wall layer. At $z_o^+ \approx 35$ (one grid point above the interface), the periodicity of the interface condition results in a secondary peak of the two-point correlation at $L_y/2$ (i.e., $r/\delta^* \simeq 14$). This secondary peak is higher (approximately 0.93) for the thick transition case; for the thin transition, it is reduced to 0.83. In the outer layer, at $z_o^+ \approx 167$ no correlation can be observed for either interface.

To determine the thickness over which the periodicity effects are felt, Fig. 11 shows the value of the secondary peak, $R_{uu}(L_y/2)$, as a function of z after 0.4 and 2 LETOTs. The narrow-transition calculations have a very rapid decrease of the secondary peak: within 4 grid points of the interface (about half a displacement thickness) the peak has decreased by 75%. Most of the outer layer is not affected at all by the periodicity introduced by the ILU. The same behavior is observed in the correlations for the other velocity components.

Since the non-periodicity of the outer layer is essentially due to the initial conditions, it is important to determine whether the flow tends to return to a periodic state or settles into a non-periodic one. To answer this question, the time development of the secondary peak is shown in Fig. 12. The thickness of the layer over which the secondary peak is significant does not change for $tu_\tau/\delta > 1$, indicating that, after a fairly short transient, the flow does indeed settle to a non-periodic state.

The rapid loss of periodicity can also be illustrated through the instantaneous contours of the fluid-dynamic variables. In Figs. 13 and 14 the velocity contours are shown for

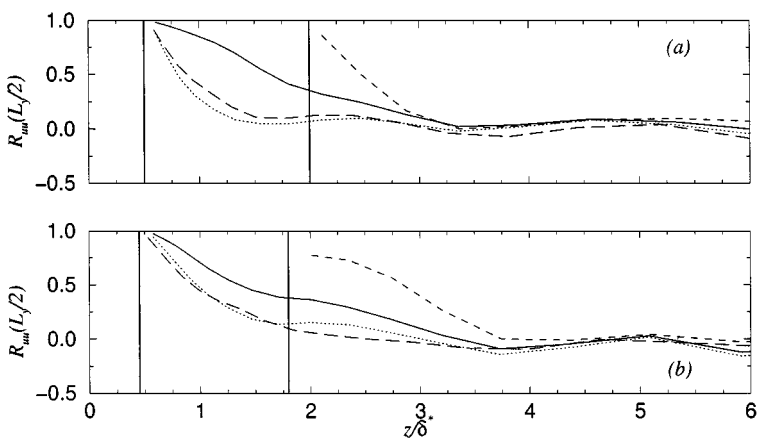

FIG. 11. Two-point spatial autocorrelation function $R_{uu}(L_y/2)$. (a) $tu_\tau/\delta^* = 0.4$, (b) $tu_\tau/\delta^* = 2$. —, $z^+_{if,o} \approx 30$, wide transition, $M = 0.3$; $\cdots$, $z^+_{if,o} \approx 30$, narrow transition, $M = 0.3$; ---, $z^+_{if,o} \approx 104$, narrow transition, $M = 0.3$; – – –, $z^+_{if,o} \approx 30$, narrow transition, $M = 0.7$. The vertical lines represent the two interfaces.

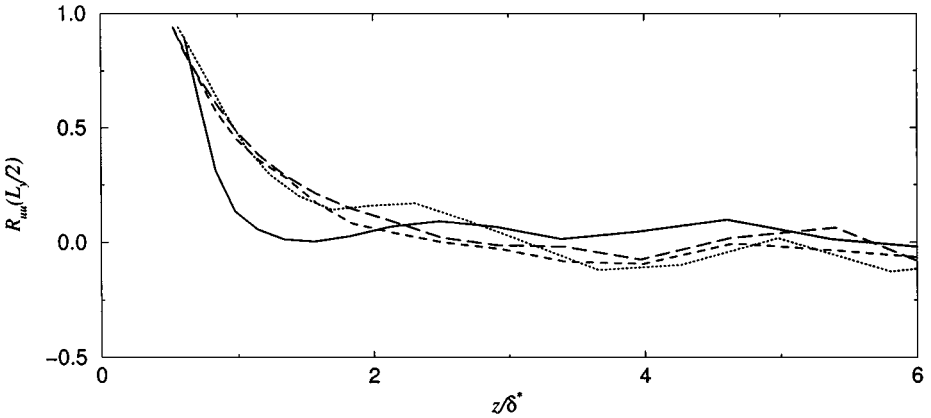

FIG. 12. Two-point spatial autocorrelation function $R_{uu}(L_y/2)$ for the $M = 0.7$ case. —, $tu_\tau/\delta = 0.1$, $\cdots$, $tu_\tau/\delta = 1$, ---, $tu_\tau/\delta = 2.$, $-\,-\,-$, $tu_\tau/\delta = 2.5$.

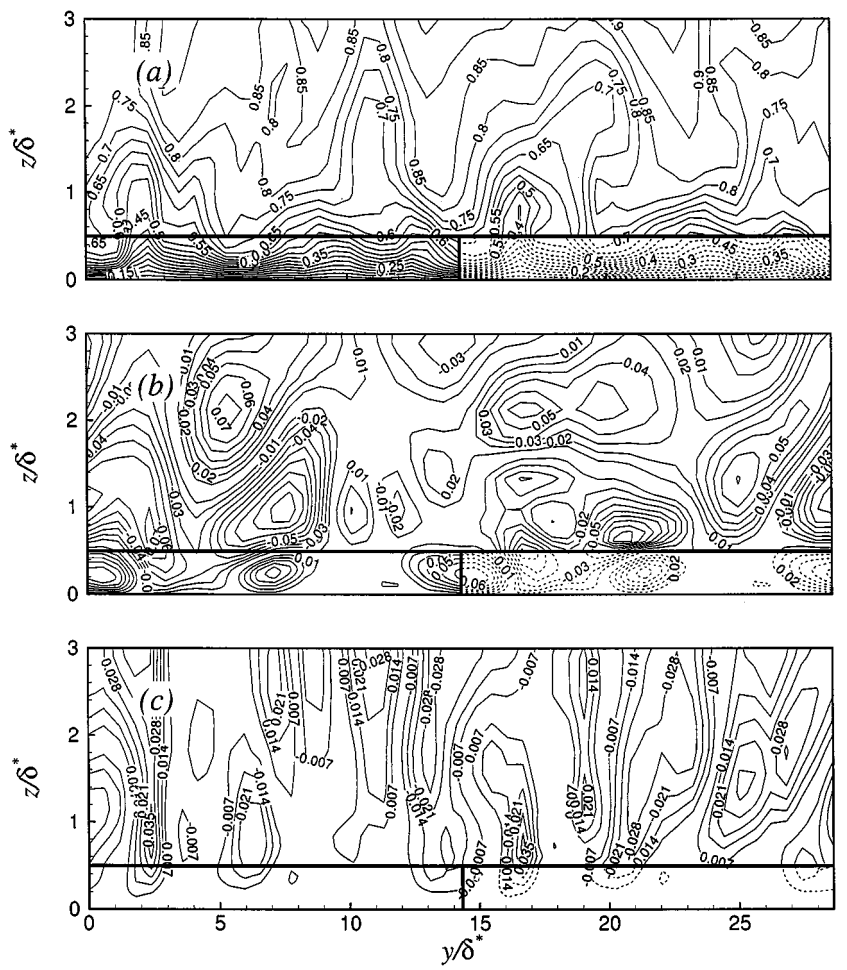

FIG. 13. Instantaneous velocity iso-contours for $M = 0.3$, $tu_\tau/\delta^* = 1$. $z^+_{if,o} \approx 30$, thin transition. (a) u; (b) v; (c) w. Dashed lines, virtual block.

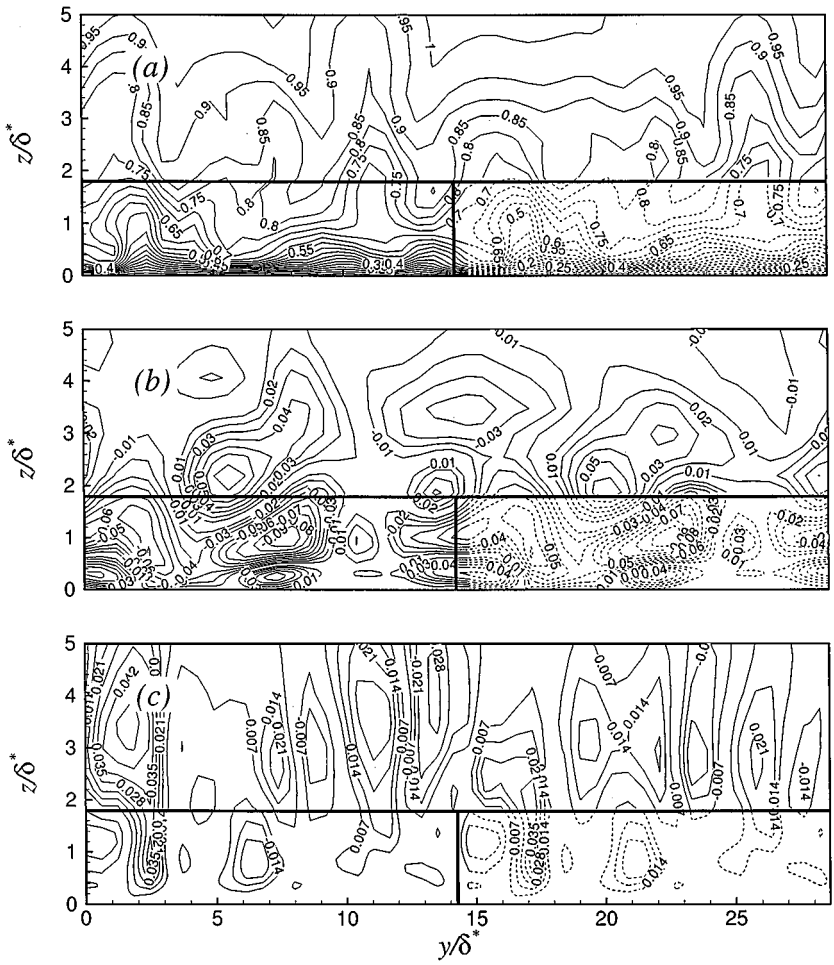

FIG. 14. Instantaneous velocity iso-contours for $M = 0.3$, $tu_\tau/\delta^* = 1$. $z^+_{if,o} \approx 104$, thin transition. (a) u; (b) v; (c) w. Dashed lines, virtual block.

the two values of the interface location. It is quite remarkable to observe the difference in the structures between the two halves of the domain. The large structure observed in the v contours at $y/\delta^* \approx 15$ and $z/\delta^* \approx 4$ in Fig. 14b is one example of a completely asymmetric eddy which must obviously result from the non-linear interactions between the wavenumbers present in the ILU and the longer wavelengths above the interface. Also notice that the high- and low-interface simulations were started from the same initial conditions; thus one would expect a similar distribution of the turbulent eddies at corresponding times. Such is the case; if Figs. 13 and 14 are compared, the large structures appear to be located roughly at the same place and have similar strength. For the different interfaces, some temporal decorrelation is caused by the modification of the initial condition. In an unstable flow such as this one, small differences in the initial conditions are amplified, and eventually lead to a complete loss of correlation. However, the statistics should not be affected, as is the case in the present calculation.

Another consequence of the modification of the initial conditions is due to the solenoidal character of the initial field. When the region corresponding to the ILU is removed, and the

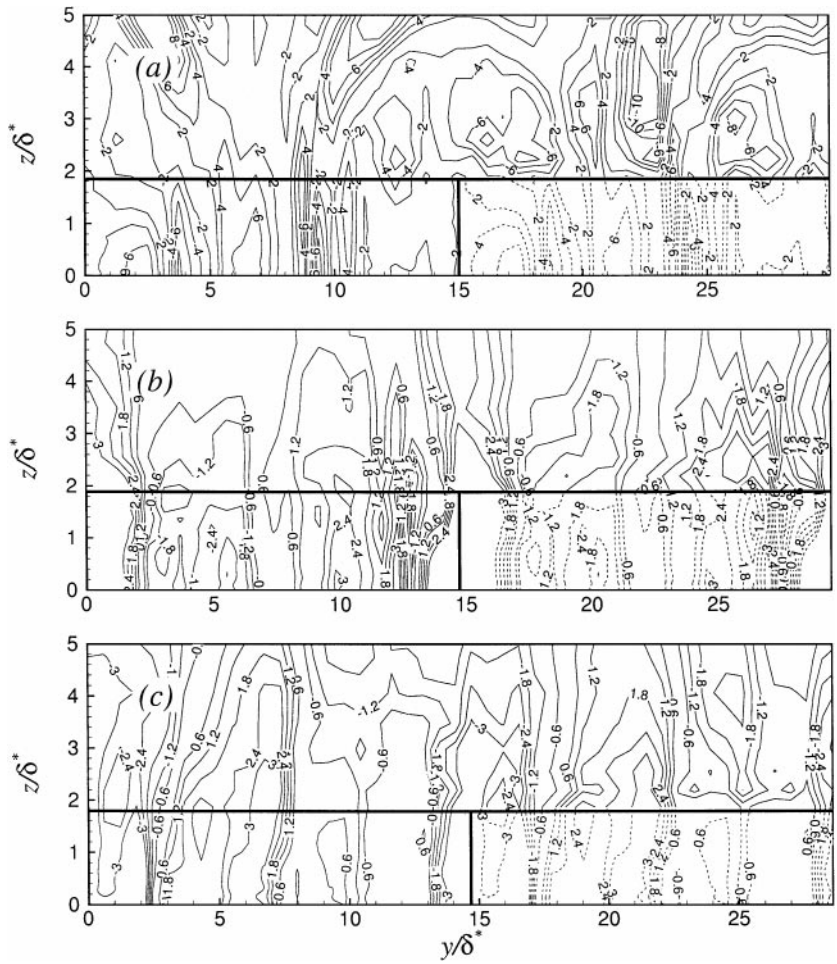

FIG. 15. Time sequence of the iso-contours of the pressure fluctuations (normalized by τ_w) for $M = 0.3$. $z^+_{if,o} \approx 104$, thin transition. (a) $tu_\tau/\delta^* = 0.01$; (b) $tu_\tau/\delta^* = 0.4$; (c) $tu_\tau/\delta^* = 1$. Dashed lines, virtual block.

velocity above it is replaced by the weighted average, the resulting initial field is no longer divergence free. This introduces a pressure disturbance at the interface between the virtual and outer-layer blocks (Fig. 15a) which decays in time (Figs. 15b and 15c). After 1 LETOT the pressure contours for the interface in the logarithmic layer have decreased in magnitude and are reasonably smooth.

When the interface is located in the buffer layer the situation is exacerbated by the fact that in a boundary layer the pressure tends to propagate unchanged across the layer. This forces a coupling between inner and outer layer in the portion of the calculation bounded by the virtual block. The ILU determines the pressure at the wall and the outer layer eddies the structure of the pressure away from the wall. This mismatch between inner and outer layer pressure fields cannot be bridged when the ILU is very thin, and some level of pressure disturbance remains throughout the simulation (Fig. 16). However, these pressure disturbances do not affect the velocity contours (shown at the same location in Fig. 13). When the interface is placed further from the wall, the flow adjusts and smoother pressure contours result.

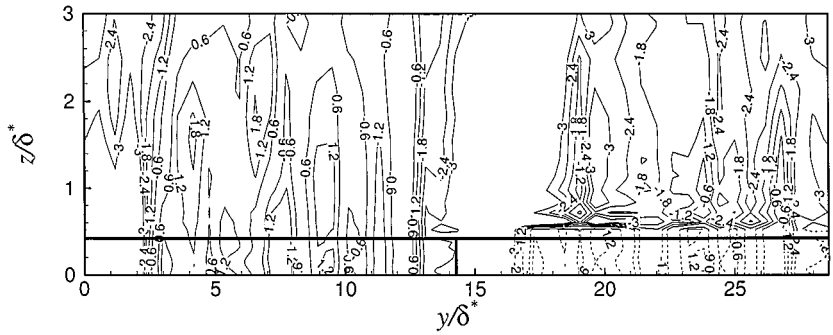

FIG. 16. Iso-contours of the pressure fluctuations (normalized by τ_w) at $tu_\tau/\delta^* = 1$. $M = 0.3$, $z^+_{if,o} \approx 30$, thin transition. Dashed lines, virtual block.

4. CONCLUSIONS

An approach for the treatment of the near-wall layer in turbulence simulations has been presented that, in flows that have one direction of homogeneity, allows substantial savings of CPU time and memory over conventional methods. This method uses computational domains whose size is determined by the local scaling. The inner layer is resolved by a sub-domain ("inner-layer unit" or ILU) whose size is fixed in wall units. The ILU is then repeated periodically as many times as required to match the dimensions of the outer layer sub-domain, which is determined by the size of the larger eddies present in the core of the flow.

Multi-block simulations with an ILU that is extended periodically give good agreement with single-block calculations for first- and second-order statistics, especially if the interface is located in the logarithmic layer. Placing the interface in the buffer layer, where much of the turbulent activity takes place, results in underprediction of the Reynolds stress magnitudes and spurious pressure fluctuations.

An important finding of this paper, that proves the feasibility of the proposed approach, is that the periodicity introduced at the interface between the inner and outer layers does not spread outwards. Within a few grid points, larger structures are generated, and the correlation between the two halves of the domain is lost.

In the present study, only modest computational savings were achieved: the two multi-block calculations required only 25 and 33% fewer points than the single-block calculation. Increases of the Reynolds number would increase the savings, but only up to a point. A multi-layer approach is required to reach higher Reynolds numbers. If non-conforming meshes of the type employed by Kravchenko *et al.* [12], for instance, are used, such that the spanwise and streamwise spacings of the outer-layers can be increased over those of the inner-layer sub-domain, additional savings can be achieved. An estimate of the possible savings can be obtained if one considers the Kravchenko *et al.* [12] calculation of plane channel flow at $Re_\tau \simeq 4{,}000$. If ILUs were used in the first three regions, each with a streamwise and spanwise domain size that is half that of the next layer, only 15% of the points used originally would be required. If the domains maintained the same streamwise length, and were reduced only in the spanwise direction, 27% of the points would be necessary.

As mentioned above, this technique requires the existence of at least one direction of homogeneity in the flow and may not be applicable in highly three-dimensional flows. However, there may be a range of intermediate configurations in which one could use periodically repeated inner-layer units in some regions of the flow only. To compute the

flow over an airplane wing, for instance, it might be possible to use periodically repeated inner layer units away from strong sources of three-dimensionality (the wing root and tip regions, the engine nacelles, etc.). Several layers, with increasing spanwise extent, non-conforming meshes would also be beneficial. Furthermore, a multiblock approach could be applied in the streamwise direction as well, joining narrower boxes to wider ones. These issues require further study.

ACKNOWLEDGMENTS

The authors thank the referees for their insightful comments. They are particularly indebted to one referee, who corrected the overly optimistic cost estimates originally presented by the authors. They also gratefully acknowledge the support from the Air Force Office of Scientific Research, under Grants AF/F49620-97-1-0244 (A.P. and U.P.) and AF/F49620-98-1-0035 (G.V.C), monitored by Dr. L. Sakell. Computer time was provided by the University of Minnesota Supercomputing Institute.

REFERENCES

1. S. K. Robinson, Coherent motions in the turbulent boundary layer, *Annu. Rev. Fluid Mech.* **23**, 601 (1991).
2. S. J. Kline, W. C. Reynolds, F. A. Schraub, and P. W. Runstadler, The structure of the turbulent boundary layer, *J. Fluid Mech.* **30**, 741 (1967).
3. J. Kim, P. Moin, and R. D. Moser, Turbulence statistics in fully-developed channel flow at low Reynolds number, *J. Fluid Mech.* **177**, 133 (1987).
4. D. R. Chapman, Computational aerodynamics development and outlook, *AIAA J.* **17**, 1293 (1979).
5. W. C. Reynolds, in *Whither turbulence? Turbulence at the Crossroads*, edited by J. L. Lumley (Springer-Verlag, Heidelberg, 1990), p. 313.
6. J. W. Deardorff, A numerical study of three-dimensional turbulent channel flow at large Reynolds numbers, *J. Fluid Mech.* **41**, 453 (1969).
7. U. Schumann, Subgrid scale model for finite difference simulation of turbulent flows in plane channel and annuli, *J. Comput. Phys.* **18**, 376 (1975).
8. U. Piomelli, J. Ferziger, P. Moin, and J. Kim, New approximate boundary conditions for large eddy simulations of turbulent channel flows, *Phys. Fluids A* **5**, 1484 (1989).
9. E. Balaras, C. Benocci, and U. Piomelli, Two-layer approximate boundary conditions for large-eddy simulations, *AIAA J.* **34**, 1111 (1996).
10. W. H. Cabot, in *Ann. Res. Briefs–1996* (Center for Turbulence Research, NASA Ames/Stanford Univ., 1996), p. 199.
11. U. Piomelli, High Reynolds number calculations using the dynamic subgrid-scale stress model, *Phys. Fluids A* **5**, 1484 (1993).
12. A. Kravchenko, P. Moin, and R. D. Moser, Zonal embedded grids for numerical simulations of wall-bounded turbulent flows, *J. Comput. Phys.* **127**, 412 (1996).
13. J. Jimenez and P. Moin, The minimal flow unit in near-wall turbulence, *J. Fluid Mech.* **225**, 213 (1991).
14. F. M. White, *Viscous Fluid Flow*, 2nd ed. (McGraw–Hill, New York, 1991).
15. A. Favre, Equations des gaz turbulents compressibles. I. Formes générales, *J. Mécanique* **4**, 361 (1965).
16. A. Favre, Equations des gaz turbulents compressibles. II. Méthods des vites moyennes; Méthode des vitesses macroscopiques pondérées par la masse volumique, *J. Mécanique* **4**, 391 (1965).
17. B. Vreman, B. Geurts, and H. Kuerten, Subgrid-modelling in LES of compressible flow, *Appl. Sci. Res.* **54**, 191 (1995).
18. M. Germano, U. Piomelli, P. Moin, and W. H. Cabot, A dynamic subgrid-scale eddy viscosity model, *Phys. Fluids A* **3**, 1760 (1991).

19. D. K. Lilly, A proposed modification of the Germano subgrid-scale closure method, *Phys. Fluids A* **4**, 633 (1992).
20. P. Moin, K. D. Squires, W. H. Cabot, and S. Lee, A dynamic subgrid-scale model for compressible turbulence and scalar transport, *Phys. Fluids A* **3**, 2746 (1991).
21. M. P. Martìn, U. Piomelli, and G. Candler, Subgrid-scale models for compressible large-eddy simulations, in *Proc. 1999 ASME Symposium on Transitional and Turbulent Compressible Flow*, 1999.
22. J. L. Steger and R. F. Warming, Flux vector splitting of the inviscid gasdynamic equation with application to finite difference methods, *J. Comput. Phys.* **40**, 263 (1981).
23. J. H. Williamson, Low-storage Runge–Kutta schemes, *J. Comput. Phys.* **35**, 48 (1980).
24. P. R. Spalart and J. H. Watmuff, Experimental and numerical study of a turbulent boundary layer with pressure gradients, *J. Fluid Mech.* **249**, 337 (1993).
25. T. S. Lund, X. Wu, and K. D. Squires, Generation of turbulent inflow data for spatially-developing boundary layer simulations, *J. Comput. Phys.* **140**, 233 (1998).
26. P. P. Sullivan, J. C. McWilliams, and C.-H. Moeng, A grid nesting method for large-eddy simutation of planetary boundary-layer flows, *Boundary-Layer Meteorol.* **80**, 167 (1996).
27. M. M. Rai, T. B. Gatski, and G. Erlebacher, *Direct Numerical Simulation of Transition and Turbulence in a Spatially Evolving Boundary Layer*, AIAA Paper No. 95-0583, 1995.
28. D. J. Olejniczak, *Direct Numerical Simulations of Compressible Turbulent Boundary Layers Using Hybrid Methods*, Ph.D. Thesis, University of Minnesota, 1998.